



On-chip stackable dielectric laser accelerator

Bin Sun^{1,2,3} · Yang-Fan He^{2,3} · Ruo-Yun Luo⁴ · Tai-Yang Zhang⁵ · Qiang Zhou^{4,6} · Shao-Yi Wang^{2,3} · Jian Zheng^{1,7,8} · Zong-Qing Zhao²

Received: 24 June 2022 / Revised: 4 November 2022 / Accepted: 14 November 2022 / Published online: 22 February 2023

© The Author(s), under exclusive licence to China Science Publishing & Media Ltd. (Science Press), Shanghai Institute of Applied Physics, the Chinese Academy of Sciences, Chinese Nuclear Society 2023

Abstract

In this paper, we propose a novel stacked laser dielectric acceleration structure. This structure is based on the inverse Cherenkov effect and represented by a parametric design formulation. Compared to existing dielectric laser accelerators relying on the inverse Smith–Purcell effect, the proposed structure provides an extended-duration synchronous acceleration field without requiring the pulse front tilting technique. This advantage significantly reduces the required pulse duration. In addition, the easy to integrate layered structure facilitates cascade acceleration, and simulations have shown that low-energy electron beams can be cascaded through high gradients over extended distances. These practical advantages demonstrate the potential of this new structure for future chip accelerators.

Keywords Dielectric laser accelerator · Inverse Cherenkov effect · Laser-driven particle acceleration

1 Introduction

The industrial applications of modern particle accelerators have been extended beyond scientific research [1, 2]. However, radio-frequency particle accelerators are typically bulky and heavy with limited practical limitations, such as the threshold for metallic structure breakdown and

restrictions in the power and wavelength of microwave sources [3–6]. In recent decades, researchers have attempted to construct miniature and even benchtop particle accelerators [7–15]. Acceleration mechanisms based on laser-dielectric interactions have recently attracted increased attention, with their promising potential to achieve the development of on-chip microscopic accelerators. The inverse Smith–Purcell effect dielectric laser accelerator (ISP-DLA) [8–15] and the inverse Cherenkov effect dielectric laser accelerator (ICS-DLA) [16–19] are two laser dielectric acceleration concepts that have been investigated since the 1960s, shortly after the invention of the laser.

This work was supported by the National Natural Science Foundation of China (Nos. 12004353, 11975214, 11991071, 11905202, and 12174350), Key Laboratory Foundation of the Sciences and Technology on Plasma Physics Laboratory (No. 6142A04200103), and Independent Scientific Research (No. JCKYS2021212011).

✉ Bin Sun
binsun97@mail.ustc.edu.cn
Jian Zheng
jzheng@ustc.edu.cn
Zong-Qing Zhao
zhaozongqing99@gmail.com

¹ CAS Key Laboratory of Geospace Environment, Department of Plasma Physics and Fusion Engineering, University of Science and Technology of China, Hefei 230026, China

² Laser Fusion Research Center, CAEP, P. O. Box 919 986, Mianyang 621900, China

³ The Sciences and Technology on Plasma Physics Laboratory, CAEP, Mianyang 621900, China

⁴ Institute of Fundamental and Frontier Sciences, University of Electronic Science and Technology of China, Chengdu 610054, China

⁵ Department of Nuclear, Plasma, and Radiological Engineering, University of Illinois at Urbana-Champaign, 104 South Wright Street, Urbana, IL 61801, USA

⁶ CAS Key Laboratory of Quantum Information, University of Science and Technology of China, Hefei 230026, China

⁷ IFSA Collaborative Innovation Center, Shanghai Jiao Tong University, Shanghai 200240, China

⁸ CAS Center for Excellence in Ultra-Intense Laser Science, Shanghai 201800, China

Most dielectric laser accelerator (DLA) schemes are based on the inverse Smith–Purcell effect. In their typical configuration, a periodic dielectric structure is adopted to spatially modulate the incident laser field and synchronize the incident-free electrons. This is achieved through the spatial harmonics of the induced waves in the electron beam channel. These previous developments have several challenges [8–15], including the following: (1) microscale fabrication of accelerator structures, which requires advanced micro-processing and nano-processing techniques; (2) selection of dielectric materials, some of which have high laser damage thresholds but cannot be fabricated as microstructures and nanostructures; (3) reduced laser damage thresholds of dielectric materials after nano-processing; (4) the pulse front tilting technique, which is required to extend the action time of the laser and dielectric to achieve extended acceleration, improve laser energy utilization efficiency, and prevent unnecessary high energy loads on the structure [20]. These challenges limit the acceleration gradient, acceleration distance, energy utilization efficiency, and flexibility of laser–dielectric acceleration structures while increasing experimental difficulty.

In this study, a stacked acceleration structure based on the inverse Cherenkov effect was developed to achieve cascade acceleration of nonrelativistic low-energy electrons through a multilayer dielectric. First, the proposed structure is identical to the existing inverse Cherenkov effect accelerator and provides effectively solves the challenges encountered in the acceleration structure of the inverse Smith–Purcell effect, including (1) elimination of the requirement for laser frontier technology and (2) not requiring multiple lasers to achieve cascade acceleration, eliminating the difficulty of coupling multiple lasers. Second, this structure considers higher acceleration gradients and energy gains and has no theoretical upper limit

on acceleration energy. In addition, because this stackable structure can be assembled from modular acceleration units, it provides additional configuration flexibility to satisfy specific requirements for different applications. This flexibility of the stackable design makes the current structure a prototype for future chip accelerators in universal application scenarios.

2 Theory and structural design

The proposed stacked acceleration structure is depicted in Fig. 1. A case study of two dielectric layers is presented in this paper for demonstration without loss of generality. The line-shaped collimated incident laser was perpendicular to Surface II and the beveled surface of a multilayer dielectric prism with a right-angled triangular cross section. An evanescent wave is generated at Surface I with a velocity of $v_p = c/(n \cdot \sin \alpha)$, traveling forward along the surface in the x -direction, where α is the angle between the hypotenuse and the bottom edge, c is the velocity of light in vacuum, and n is the refractive index of the prism. This wave has a longitudinal electric field component E_x , transverse electric field component E_y , and out-of-plane magnetic field component B_z .

The electrons move in the x -direction in the vacuum below Surface I. Electrons in phase with an accelerating electric field (equivalently, negative phase $E_x < 0$) can then be accelerated by applying the inverse Cherenkov effect. However, the electron velocity v_e must be equal to that of the evanescent wave, that is, $v_e = v_p$, to achieve continuous acceleration. On Surface I, the first criterion [17–19] for achieving continuous acceleration through the inverse Cherenkov effect is:

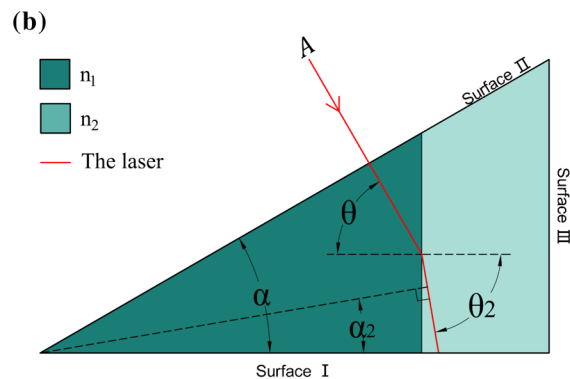
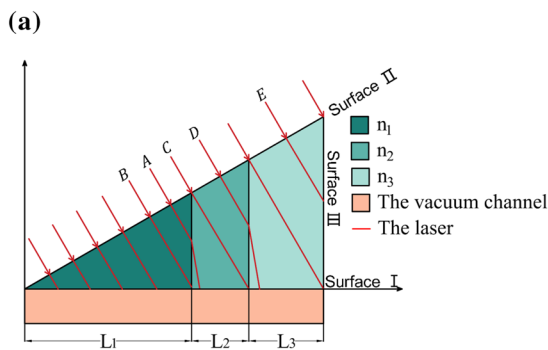


Fig. 1 (Color online) **a** Schematic of stacked acceleration structure. The red arrow line represents the incident laser. The refractive indices of the two dielectric layers are n_1 and n_2 . **b** Partial enlargement of Fig. 1a showing refraction process occurring at interface. The angles

between the bottom edge of the right-angled triangle and the two transversal directions perpendicular to two laser beams (equivalently, the electric field directions) are α and α_2 , respectively

$$\sin \alpha = c/(v_e n) = 1/(\beta n). \tag{1}$$

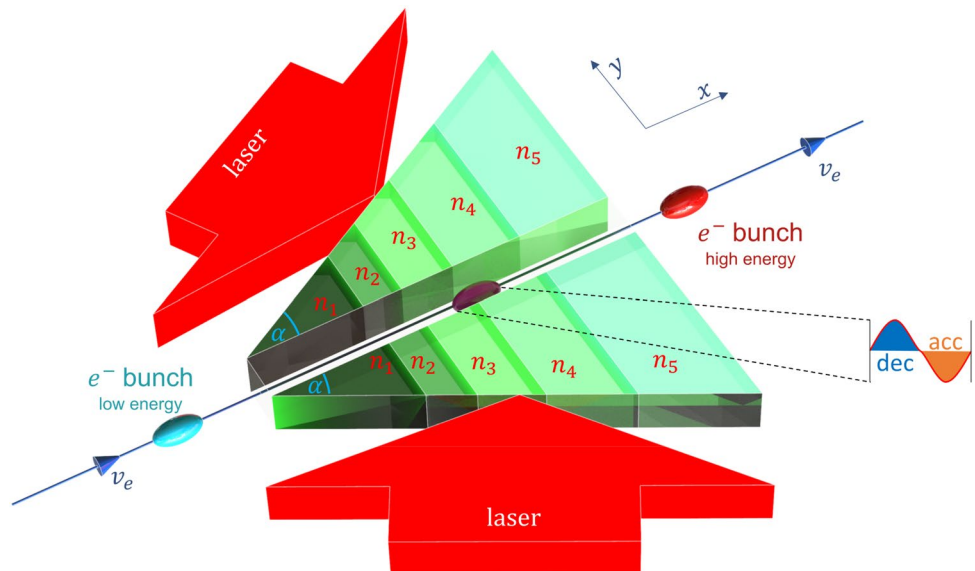
In Eq. (1), α is the angle between the hypotenuse and the bottom edge, c and v_e are the velocities of the light in vacuum and electrons, respectively, and $\beta = v/c$ is the relativistic velocity of the electron. As the electron accelerates and v_e increases, the electrons move faster than the wave, lose synchronization, and eventually, their acceleration end. Currently, the solution to this problem is achieved by varying angle α [18, 19]. In this study, the electron velocity was matched to the wave velocity by selecting a different dielectric to vary the refractive index. First, the refracted light ray A is analyzed, as shown in Fig. 1. Each time the laser passes through the interface between two adjacent layers with different dielectrics, the light is refracted owing to a change in the refractive index. Some of the laser light is reflected, which reduces the laser energy; this reduction is undesirable for the energy utilization efficiency and accelerating electric field. Thus, it is necessary to ensure that the light passes through the interface only once so that the laser experiences only one additional reflection and refraction. A limit was proposed for the dielectric length of each layer to achieve this. Taking the second layer in Fig. 1 as an example, the second layer thickness L_2 is limited by Rays B and C. The geometric relationship is expressed by $L_2 = L_1 \times (\tan \alpha)^2$. Similarly, the recurrence equation for the thickness L_i of each subsequent layer can be derived, $L_{i+1} = L_i/(\cos \alpha)^2, i \geq 2$. By combining these two equations, the relationship between the thickness L_i of each layer and the thickness L_1 of the first layer is expressed by $L_i = L_1 \times (\tan \alpha)^2/(\cos \alpha)^{2(i-2)}, i \geq 2$. Second, even when the laser passes through the interface only once, as shown in Fig. 1, the angle of the laser to the bottom surface (Surface I) changes from α to α_2 after refraction at the dielectric

interface. Equation (1) must still be satisfied to maintain acceleration: $\sin \alpha_2 = 1/(\beta_2 n_2)$. When refraction occurs at the interface, the law of refraction is expressed by $n_1 \sin \theta_1 = n_2 \sin \theta_2$. In addition, the trigonometric relationship is $1 = (\sin \alpha_2)^2 + (\cos \alpha_2)^2 = [1/(\beta_2 n_2)]^2 + (\sin \theta_2)^2 = [1/(\beta_2 n_2)]^2 + (n_1 \sin \theta_1/n_2)^2$. Solving these equations yield n_2 , where $n_2 = [(n_1 \sin \theta_1)^2 + \beta_1^{-2}]^{1/2}$. A similar derivation holds at each interface, resulting in the recurrence relationship $n_i = [(n_{i-1} \cdot \sin \theta_{i-1})^2 + \beta_i^{-2}]^{1/2}, i \geq 2$. In addition, because the incidence angle of the laser is the same for each layer of the dielectric, $\theta_1 = \theta_2 = \dots = \theta_n = \pi/2 - \alpha$, the recurrence relationship can be simplified to $n_i = [(n_{i-1} \cdot \sin \theta_{i-1})^2 + \beta_i^{-2}]^{1/2} = [(n_{i-1} \cdot \cos \alpha)^2 + \beta_i^{-2}]^{1/2}, i \geq 2$. In summary, the refractive index and thickness of each layer of the dielectric, starting from the second layer, can be derived as a function of the parameters of the first layer.

$$\begin{cases} n_i = [(n_{i-1} \cdot \cos \alpha)^2 + \beta_i^{-2}]^{1/2} \\ L_i = L_1 \times (\tan \alpha)^2/(\cos \alpha)^{2(i-2)}, i \geq 2 \end{cases} \tag{2}$$

In the first row of Eq. (2), n_i is the refractive index of the layer, and the label, i , follows the convention in Figs. 1 and 2. β_i is the theoretical design velocity of electrons in the vacuum acceleration region on Surface I below the i th layer of the dielectric, which is also the velocity of light in the x -direction when it is in this dielectric. For this theoretical electron velocity, as the electron beam stream advances longitudinally in the acceleration channel, the electron energy and velocity increase. Electron velocity v_e gradually increases when the electron moves below the surface of each dielectric layer, whereas the velocity v_0 of the corresponding laser pulse remains unchanged. Therefore, the phase

Fig. 2 (Color online) Schematic of structure of 50 keV electron acceleration. The light blue, purple, and red ellipses represent the injected low-energy (50 keV) electron beam stream, accelerating electron beam stream (schematic), and output high-energy electron beam stream, respectively. The insertions “dec” and “acc”, indicate that half of the phases in a laser cycle accelerate the electrons, and the other half decelerate them



difference gradually accumulates as the electrons move with the laser during the acceleration phase, $\Phi = \omega t(1 - n\beta \sin \alpha)$. If the electron beam is injected at the maximum amplitude of the laser, it becomes necessary to ensure that the phase difference $|\Phi| \leq \pi/2$ when the electron beam leaves; otherwise, it enters the deceleration phase. This corresponds to two cases. (1) The electron velocity v_e is extremely high, resulting in phase difference $\Phi \leq -\pi/2$, and the electron beam reaches the front deceleration phase. (2) The electron velocity v_e is extremely low, resulting in phase difference $\Phi \geq \pi/2$, and the electron beam will enter the rear deceleration phase.

A suitable electron beam velocity, as expressed by Eq. (3), can be selected to extend the acceleration distance and duration. This is achieved such that (1) the electron beam velocity is lower than the speed of light in the dielectric at the entrance of each dielectric layer, and (2) the electron beam velocity is higher than the speed of light in the dielectric at the exit of each dielectric layer. In Eq. (3), x_e is the longitudinal position of the electron, n is the entry into the n th layer of the dielectric, and $\sum_{i=1}^{n-1} L_i = 0$ when $n = 1$. Thus, the relative longitudinal displacement of the electron beam stream in the phase is first backward (equivalently, the negative x -direction) and then forward (equivalently, the positive x -direction), extending the duration in the accelerated phase [9, 15].

$$\begin{cases} v_e < v_o, x_e = \sum_{i=1}^{n-1} L_i \\ v_e > v_o, x_e = \sum_{i=1}^n L_i \end{cases} \quad (3)$$

In the second row of Eq. (2), L_i is the thickness of the layers, known as L_1 and L_2 in Fig. 1. From recursive formula (2), as long as the prism base angle α , refractive index n_1 , and thickness L_1 of the first layer of the dielectric are specified, the remaining refractive index n_i and thickness L_i can be obtained recursively. Moreover, Eq. (1) indicates that when the incident electron energy is determined, only one degree of freedom remains between α and n_1 . Generally, researchers tend to select quartz and other common materials within the range of refractive indices and make the base angle α as small as possible. A positive correlation exists between the acceleration electric field or acceleration gradient and $\cos \alpha$; hence, a smaller base angle α indicates a higher acceleration gradient [17–19]. In addition, the continuous or arbitrary regulation of the dielectric refractive index has led to significant progress in research on optical materials; therefore, a dielectric satisfying Eq. (2) can be fabricated [21–23].

Based on the theoretical analysis above, a two-dimensional numerical simulation study was conducted using the finite element method and the particle-in-cell algorithm. The simulated structure is shown in Fig. 2. The base angle

α of the prism was set to 30° , and the refractive index and thickness of each layer were calculated using Eqs. (2) and (3), respectively. A symmetric double prism was used, in which the transverse forces on both sides of the channel centerline are of equal magnitude but in opposite directions. This configuration prevents beam deflections. The geometric parameters of the simulated structures are listed in Table 1. The laser was set as a 10.00- μm far-infrared CO_2 laser. Because the timescale of the simulated physical process is similar to the pulse width of widely used CO_2 lasers [24–28], the laser was set as a continuous plane wave with an electric field amplitude of $E_0 = 5.0 \text{ GV} \cdot \text{m}^{-1}$. The selected value implies that the power density of the laser beam is approximately $6.6 \times 10^{12} \text{ W/cm}^2$, and the energy density of the laser pulse irradiating the prism is approximately 0.2 J/cm^2 . These values are consistent with the laser parameters used in a related study [17]. We propose that line-shaped laser pulses collimated by a cylindrical lens be utilized to drive the symmetric prism, enabling long-distance synchronization. With an energy of 50.00 keV, the injected electrons were in the low-energy nonrelative range ($\beta \ll 1$) typical for monoenergetic electron beams generated from electron guns with no initial energy dispersion and a charge of 9.36 fC. The particles in the bunch followed a KV distribution. The KV distribution uniformly places the particles in the phase space. The distance between the particles was approximately the same throughout the beam. The initially normalized emittance was $10^3 \text{ pm} \cdot \text{rad}$. The initial maximum transverse distance relative to the center of the beam was $0.1 \mu\text{m}$, and the maximum divergence angle was approximately 23 mrad. The longitudinal beam length was 3.34 fs, and the distance between the center of the electron beam and prism Surface I was $0.5 \mu\text{m}$. These design parameters are consistent with those of the electron beam generated using the electron gun of the DLA [29–31], and the covered parametric range has not yet been investigated for the inverse Cherenkov effect particle accelerator [16–19].

Table 1 Simulation parameters of geometric structure

Section	Length (μm)	Refractive index
First	31.31	3.96
Second	10.44	3.74
Third	13.92	3.56
Fourth	18.56	3.40
Fifth	24.74	3.21
Structural spacing	1.00	1.00

3 Simulation results and discussion

The energy spectrum of the accelerated electron beam stream is shown in Fig. 3a. Figure 3a corresponds to the instant at 600.42 fs. Here, the electron beam had completely accelerated. The peak energy was 309.55 keV, and the full-width at half-maximum (FWHM) of the energy dispersion was 2.00 keV, corresponding to a relative ratio of 0.65%. Correspondingly, an electron energy gain of 259.55 keV was achieved with an average acceleration gradient of 2.62 GeV m^{-1} and an acceleration factor $E_{\text{acc}}/E_0 \approx 0.52$. This was obtained by dividing the total energy gain of the electrons by the entire path length of approximately $98.96 \mu\text{m}$. The phase space diagram of the horizontal (y -direction) space is shown in Fig. 3b, which corresponds to the same moment as in Fig. 3a. The maximum divergence angle of the electron beam did not exceed 21 mrad. Compared with the initial value of approximately 23 mrad, the divergence angle was reduced, and a weak focusing effect was achieved. Figure 3c shows the spatial

(x -direction) of the electron beam and the energy distribution with time, with the sampling points separated by $0.25T_0$ or approximately 8.34 fs. The electron energy increased monotonically, and continuous acceleration was achieved. The curve representing the electron beam energy increased smoothly through the vacuum channel, with only some jitter at the layer interfaces. This smooth increase indicates that the acceleration gradient does not change significantly at each stage; thus, the proposed stacked acceleration structure achieves long-range acceleration with a high acceleration gradient. The electron beam underwent diffusion and recompression in the spatial x -direction, and the energy of the electron beam underwent diffusion and recompression. The stretched and diffused of the electron beam are caused by inhomogeneous field distribution in the accelerated vacuum channel, as reported in the literature [17–19]. When the diffusion of the electron beam stream becomes very strong, the positive phase ($E_x > 0$), that is, the decelerating phase electric field in front and behind the electron beam, suppresses it, introducing negative feedback. Consequently, the

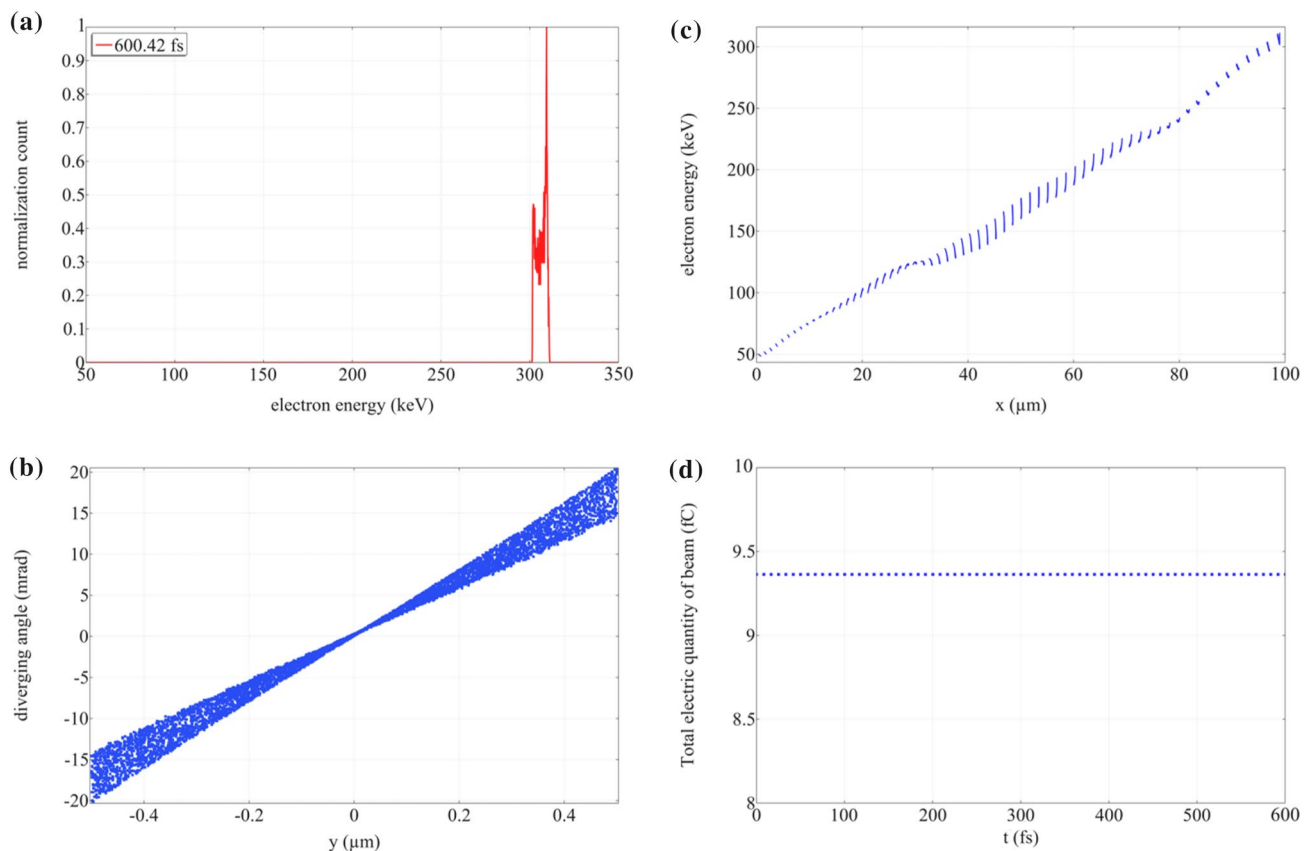


Fig. 3 (Color online) **a** Electron energy spectrum at end of acceleration, normalized to peak. **b** Phase space diagram of horizontal (y -direction) space. The vertical coordinate is the divergence angle, and the horizontal coordinate is the lateral position of the electron.

c Spatial (x -direction) and energy distribution of electron beam at each moment (difference of $0.25T_0$ for each data sampling point). **d** Total power variation in electron beam at each moment (difference of $0.25T_0$ for each data sampling point)

length of the accelerated electron beam is limited to half of the laser cycle, and the extremely fast electrons slow down, inhibiting their energy increment and minimizing the energy dispersion. This also reduces the speed of the fast electron beams and concentrates the electrons in the movement direction. This technique facilitates the electron beam to achieve its quasi-monoenergy and compression in the direction of motion after passing through the channel. This property may be valuable in future ultrashort pulse electron beam streams such as attosecond pulses, ultrafast electron diffraction, and other fields. In addition, the electron charge for the fluctuation of the electron beam current charge was observed (Fig. 3d), and the simulation demonstrated that no beam loss occurred during the electron beam current acceleration. This finding is consistent with the earlier analysis that the field generated by this stacked structure does not cause transverse (y -direction) deflection of the electron beam current. Furthermore, the width of such a vacuum channel is adequate.

The spatial and temporal variations in the longitudinal electric field E_x along the central axis of the vacuum channel were investigated to further examine the acceleration process of the electron. The path of an electron carrying average energy was adopted to approximate the mean trajectory of the electron beam, as shown in Fig. 4. This demonstrates how an electric field induces electron acceleration or deceleration. The blue–violet region represents the deceleration field, whereas the orange–red zone represents the acceleration field. The net energy gain of a particle is closely related to the phase in which the electron beam is placed in the electric field, E_x . In the phase of the laser electric field, the solid green line represents the global line of the particle beam with average velocity. The electron

beam is synchronized with the laser pulse and is always in the negative phase of the electric field ($E_x < 0$), known as the acceleration phase. This is why a stacked structure can achieve a high acceleration gradient for long-distance acceleration. Accelerating a single beam does not fully utilize all the acceleration phases. Therefore, in the future, a multibeam cluster acceleration mode similar to modern conventional accelerators, with each pair of neighboring electron beam clusters spaced by a deceleration phase, can be adopted to improve the energy conversion efficiency and electron beam power.

Moreover, the performance of each layer of the structure was assessed to adapt it to future chip accelerator applications and construct a structure that can be dismantled to alter the electron beam energy to satisfy the needs of various situations. The energy spectrum of the electron beam stream produced by the acceleration of each layer is shown in Fig. 5. The moments indicated by different colors in Fig. 5 correspond to the electron energy spectra obtained from the first layer to the sixth layer of the dielectric acceleration. The values are listed in Table 2. The energy dispersion of the intermediate electron beam flow was relatively high. However, none of the energy dispersions exceeded 4.00 keV of the FWHM, and none of the corresponding relative ratio values exceeded 2.00%. The peak energy of the electron beam obtained from the final acceleration was 309.55 keV, and the FWHM of the energy dispersion did not exceed 2.00 keV. This indicates that the intermediate electron beam flow can also be used as the injection step, as discussed in the next section.

Table 2 presents the results of an investigation of the acceleration efficiency, in which the energy gain in the electron beam stream in each accelerated stage is determined,

Fig. 4 (Color online) Electric field E_x (magnitude normalized with respect to E_0) as functions of time and space (x -position). The vector of this field is in the lateral direction of the vacuum channel. The green line indicates the electron trajectory, and the sampling time step is $0.25T_0$. The color bar on the right represents the normalized field strength, E_x/E_0 ratio

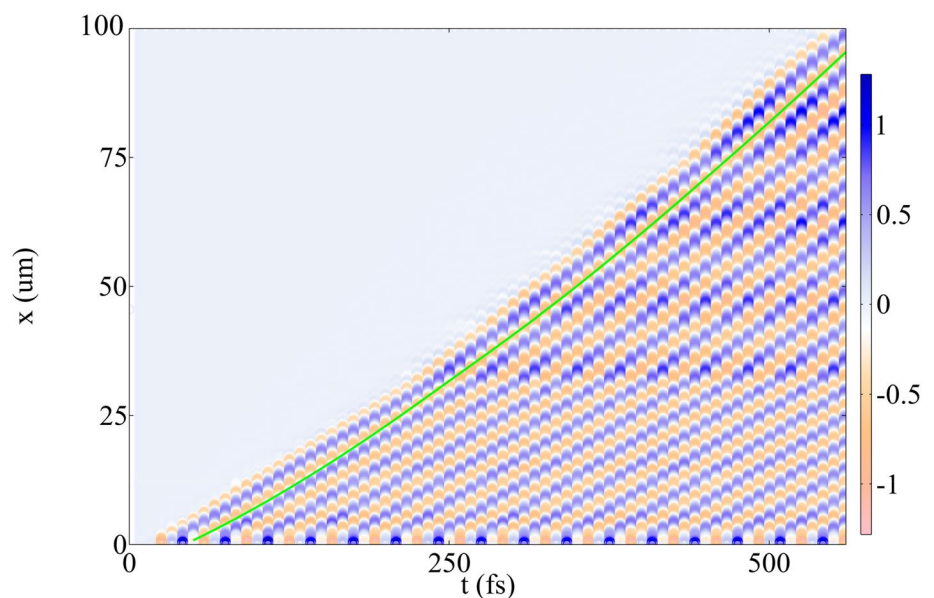


Fig. 5 (Color online) Electron beam energy spectrum corresponding to end of acceleration of each layer of dielectric

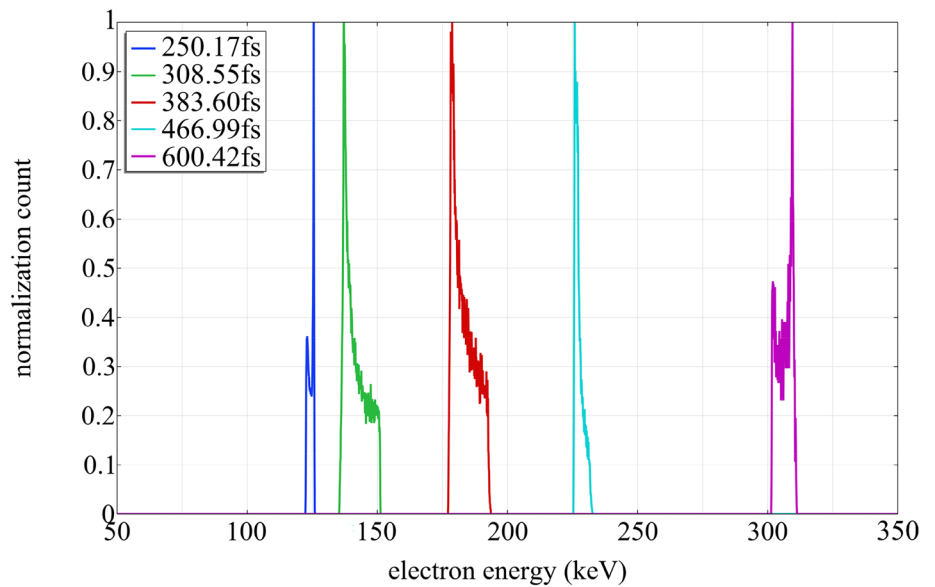


Table 2 Electron beam profile and acceleration performance for each layer

Section	Electron energy (keV)	Half-height-width (keV)	Ratio (%)	Electron gain energy (keV)	Average acceleration gradient ($\text{GeV} \cdot \text{m}^{-1}$)
First	125.55	0.34	0.27	75.55	2.41
Second	137.15	2.40	1.75	11.60	1.11
Third	178.75	3.53	1.97	41.60	2.99
Fourth	225.85	1.67	0.74	47.10	2.54
Fifth	309.55	2.00	0.65	83.70	3.38
Total	309.55	2.00	0.65	259.55	2.62

Table 3 Size of subsequent structure

Section	Length (μm)	Height (μm)
Sixth	32.99	76.18
Seventh	43.98	101.58
Eighth	58.64	135.44
Ninth	78.19	180.58
Tenth	104.26	240.78

together with the corresponding average acceleration gradient. This coincided with the case presented in Fig. 3c.

This section presents the expandability of the proposed structure. First, the acceleration distance required to accelerate a 50 keV electron beam to 1 MeV was approximately $362.60 \mu\text{m}$ using an average acceleration gradient of $2.62 \text{ GeV} \cdot \text{m}^{-1}$ for the entire structure. Second, the thickness and refractive index of the dielectric to be added could be obtained using Eqs. (2) and (3). The length (x-direction or Surface I direction) and height (y-direction

or Surface III direction, the highest point of the prism) of each subsequent layer are listed in Table 3. In this case, the acceleration structure of the first five segments used the above structure. Furthermore, preliminary estimates were obtained for longer acceleration distances and higher energy gains. The electron relativistic velocity β and dielectric refractive index n changed with increasing electron energy (Fig. 6a). The pinch angle was based on the same initial angle as used in this study. The refractive index of the dielectric rapidly decreased as the electron energy increased, and the refractive index eventually reached 2.00 and remained constant. Figure 6b shows the variation in the thickness of each section of the dielectric structure. The thickness of each stage increased exponentially as the number increased. Dielectrics of this size are easy to prepare. In addition, the laser could be infinitely extended in one direction (with the focal length or extendable distance significantly longer than the acceleration distance) and tightly focused in the other direction (laser wavelength magnitude) using beam spreading and line-shaped

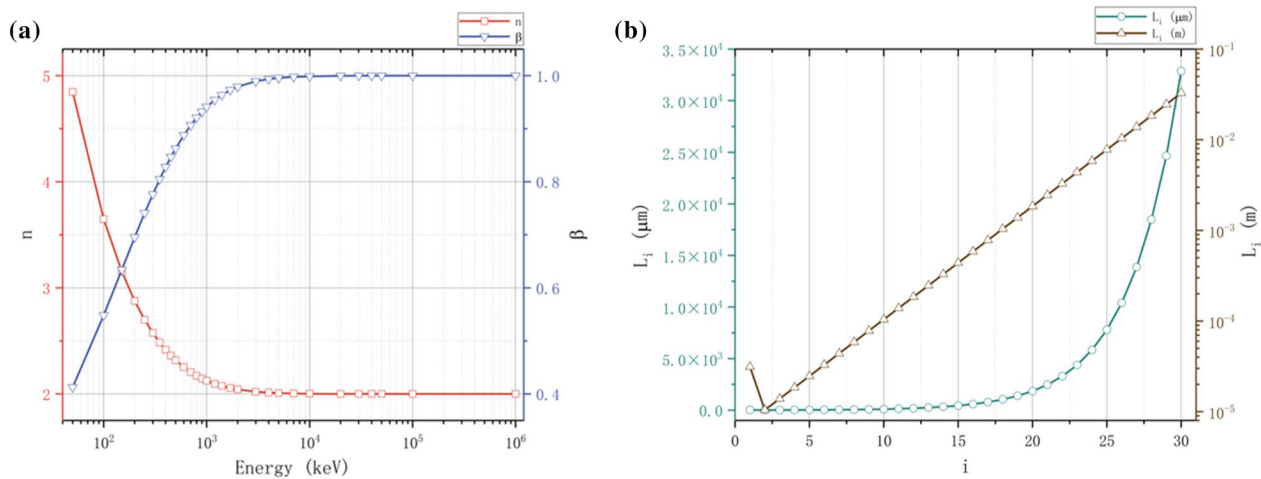


Fig. 6 (Color online) **a** Electron relativistic velocity (blue line) and dielectric refractive index (red line) as functions of electron energy; **b** length of each section of dielectric structure (The green and brown

lines indicate measurements in microns and meters, respectively, while logarithmic coordinates are used.)

collimation [32]. This implies that on Surfaces I and II (Fig. 1), the passing distance of the laser in the dielectric is significantly longer than the required acceleration distance. In general, the proposed structure can be extended to higher energy targets by adding a new dielectric layer behind the structure.

4 Conclusion

A laser dielectric accelerator is proposed based on the inverse Cherenkov phenomenon using a multilayer structure. A parametric design approach was applied to this structure and is demonstrated with a design example for accelerating electron beam currents ranging from 50.00 to 309.55 keV. This suggests that the stackable structure requires a high-energy-gain cascade acceleration technique featuring a high acceleration gradient and an extended acceleration distance, as demonstrated via the simulation. Furthermore, this stackable accelerating structure has a flexible configuration. Theoretically, the structure can achieve arbitrarily high acceleration under design assumptions by extending the accelerator length following the proposed design procedure. The proposed structure is a promising prototype for use in future chip accelerators.

Acknowledgements The authors thank Prof. Du Wang of Wuhan University, Prof. Wen Luo of the University of South China, Post-doc Yi-Ming Pan of Technion-Israel Institute of Technology, Dr. Bin Zhao of Tel Aviv University, Dr. Wei Li of the University of Science and Technology of China, and Dr. Lai Wei of Laser Fusion Research Center, CAEP, for the insightful discussion. The authors also thank the anonymous reviewers for their constructive comments.

Author contributions All authors contributed to the study conception and design. Material preparation, data collection and analysis were performed by Bin Sun, Yang-Fan He and Ruo-Yun Luo. The first draft of the manuscript was written by Bin Sun and all authors commented on previous versions of the manuscript. All authors read and approved the final manuscript.

References

1. Y. Zhang, W.-C. Fang, X.-X. Huang et al., Design, fabrication, and cold test of an S-band high-gradient accelerating structure for compact proton therapy facility. *Nucl. Sci. Tech.* **32**, 38 (2021). <https://doi.org/10.1007/s41365-021-00869-z>
2. W. Nan, B. Guo, C.-J. Lin et al., First proof-of-principle experiment with the post-accelerated isotope separator on-line beam at BRIF: measurement of the angular distribution of $^{23}\text{Na} + ^{40}\text{Ca}$ elastic scattering. *Nucl. Sci. Tech.* **32**, 53 (2021). <https://doi.org/10.1007/s41365-021-00889-9>
3. Z.-Y. Ma, S.-J. Zhao, X.-M. Liu et al., High RF power tests of the first 1.3 GHz fundamental power coupler prototypes for the SHINE project. *Nucl. Sci. Tech.* **33**, 10 (2022). <https://doi.org/10.1007/s41365-022-00984-5>
4. B. Naranjo, A. Valloni, S. Putterman et al., Stable charged-particle acceleration and focusing in a laser accelerator using spatial harmonics. *Phys. Rev. Lett.* **109**, 164803 (2012). <https://doi.org/10.1103/PhysRevLett.109.164803>
5. E.A. Peralta, K. Soong, R.J. England et al., Demonstration of electron acceleration in a laser-driven dielectric microstructure. *Nature* **503**, 91–94 (2013). <https://doi.org/10.1038/nature12664>
6. R.J. England, R.J. Noble, K. Bane et al., Dielectric laser accelerators. *Rev. Modern Phys.* **86**, 1337–1389 (2014). <https://doi.org/10.1103/RevModPhys.86.1337>
7. Y.-F. He, B. Sun, M.-J. Ma et al., Topology optimization of on-chip integrated laser-driven particle accelerator. *Nucl. Sci. Tech.* **33**, 120 (2022). <https://doi.org/10.1007/s41365-022-01101-2>

8. K.J. Leedle, R.F. Pease, R.L. Byer et al., Laser acceleration and deflection of 9.63 keV electrons with a silicon dielectric structure. *Optica* **2**, 158–161 (2015). <https://doi.org/10.1364/OPTICA.2.000158>
9. K.P. Wootton, Z.R. Wu, B.M. Cowan et al., Demonstration of acceleration of relativistic electrons at a dielectric microstructure using femtosecond laser pulses. *Opt. Lett.* **41**, 2696–2699 (2016). <https://doi.org/10.1364/OL.41.002696>
10. J. McNeur, M. Kozák, N. Schöenberger et al., Elements of a dielectric laser accelerator. *Optica* **5**, 687–690 (2018). <https://doi.org/10.1364/OPTICA.5.000687>
11. P. Yousefi, N. Schöenberger, J. Mcneur et al., Dielectric laser electron acceleration in a dual pillar grating with a distributed Bragg reflector. *Opt. Lett.* **44**, 1520–1523 (2019). <https://doi.org/10.1364/OL.44.001520>
12. N.V. Saprà, K.Y. Yang, D. Vercruyssen et al., On-chip integrated laser-driven particle accelerator. *Science* **367**, 79–83 (2020). <https://doi.org/10.1126/science.aay5734>
13. R. Shiloh, J. Illmer, T. Chlouba et al., Electron phase-space control in photonic chip-based particle acceleration. *Nature* **597**, 498–502 (2021). <https://doi.org/10.1038/s41586-021-03812-9>
14. Y. Meng, Y. Chen, L. Lu et al., Optical meta-waveguides for integrated photonics and beyond. *Light Sci. Appl.* **10**, 235 (2021). <https://doi.org/10.1038/s41377-021-00655-x>
15. T. Chlouba, R. Shiloh, P. Forsberg et al., Diamond-based dielectric laser acceleration. *Opt. Express* **30**, 505–510 (2022). <https://doi.org/10.1364/OE.442752>
16. M. Kozák, P. Beck, H. Deng et al., Acceleration of sub-relativistic electrons with an evanescent optical wave at a planar interface. *Opt. Express* **25**, 19195–19204 (2017). <https://doi.org/10.1364/OE.25.019195>
17. W. Liu, Z. Yu, L. Sun et al., Microscale laser-driven particle accelerator using the inverse Cherenkov effect. *Phys. Rev. Appl.* **14**, 014018 (2020). <https://doi.org/10.1103/PhysRevApplied.14.014018>
18. L. Sun, W. Liu, J. Zhou et al., GV m⁻¹ on-chip particle accelerator driven by few-cycle femtosecond laser pulse. *New J. Phys.* **23**, 063031 (2021). <https://doi.org/10.1088/1367-2630/ac03cf>
19. W.H. Liu, L. Sun, Z.J. Yu et al., THz-driven dielectric particle accelerator on chip. *Opt. Lett.* **46**, 4398–4401 (2021). <https://doi.org/10.1364/OL.430451>
20. Y. Wei, M. Ibison, G. Xia et al., Dual-grating dielectric accelerators driven by a pulse-front-tilted laser. *Appl. Opt.* **56**, 8201–8206 (2017). <https://doi.org/10.1364/AO.56.008201>
21. G. Pilania, E. Weis, E.M. Walker et al., Computational screening of organic polymer dielectrics for novel accelerator technologies. *Sci. Rep.* **8**, 9258 (2018). <https://doi.org/10.1038/s41598-018-27572-1>
22. D.H. Lippman, N.S. Kochan, T. Yang et al., Freeform gradient-index media: a new frontier in freeform optics. *Opt. Express* **29**, 36997–37012 (2021). <https://doi.org/10.1364/OE.443427>
23. R. Dylla-Spears, D. Yee Timothy, K. Sasan et al., 3D printed gradient index glass optics. *Sci. Advncs* **6**, 7429 (2020). <https://doi.org/10.1126/sciadv.abc7429>
24. W.D. Kimura, I.V. Poaorelsky, L. Schächter, CO₂-laser-driven dielectric laser accelerator. In *2018 IEEE Advanced Accelerator Concepts Workshop (AAC)*, 1–5. 2018 <https://doi.org/10.1109/AAC.2018.8659403>
25. M.N. Polyanskiy, I.V. Pogorelsky, V. Yakimenko, Picosecond pulse amplification in isotopic CO₂ active medium. *Opt. Express* **19**, 7717–7725 (2011). <https://doi.org/10.1364/OE.19.007717>
26. M.N. Polyanskiy, M. Babzien, I.V. Pogorelsky, Chirped-pulse amplification in a CO₂ laser. *Optica* **2**, 675–681 (2015). <https://doi.org/10.1364/OPTICA.2.000675>
27. M.N. Polyanskiy, I.V. Pogorelsky, M. Babzien et al., Demonstration of a 2 ps, 5 TW peak power, long-wave infrared laser based on chirped-pulse amplification with mixed-isotope CO₂ amplifiers. *OSA Continuum* **3**, 459–472 (2020). <https://doi.org/10.1364/OSAC.381467>
28. P. Panagiotopoulos, M.G. Hastings, M. Kolesik et al., Multi-terawatt femtosecond 10 μm laser pulses by self-compression in a CO₂ cell. *OSA Continuum* **3**, 3040–3047 (2020). <https://doi.org/10.1364/OSAC.399992>
29. J. Hoffrogge, J. Paul Stein, M. Krüger et al., Tip-based source of femtosecond electron pulses at 30 keV. *J. Appl. Phys.* **115**, 094506 (2014). <https://doi.org/10.1063/1.4867185>
30. M. Krüger, C. Lemell, G. Wachter et al., Attosecond physics phenomena at nanometric tips. *J. Phys. B Atomic Mol. Opt. Phys.* **51**, 172001 (2018). <https://doi.org/10.1088/1361-6455/aac6ac>
31. T. Hirano, K.E. Urbanek, A.C. Ceballos et al., A compact electron source for the dielectric laser accelerator. *Appl. Phys. Lett.* **116**, 161106 (2020). <https://doi.org/10.1063/5.0003575>
32. P.A. Naik, S.R. Kumbhare, V. Arora et al., A new technique for obtaining uniform intensity line focus of Gaussian laser beams. *Opt. Commun.* **223**, 137–142 (2003). [https://doi.org/10.1016/S0030-4018\(03\)01544-X](https://doi.org/10.1016/S0030-4018(03)01544-X)

Springer Nature or its licensor (e.g. a society or other partner) holds exclusive rights to this article under a publishing agreement with the author(s) or other rightsholder(s); author self-archiving of the accepted manuscript version of this article is solely governed by the terms of such publishing agreement and applicable law.